MULTIGRID PROPERTIES OF UPWIND-BIASED DATA RECONSTRUCTIONS

Gary P. Warren and Thomas W. Roberts
NASA Langley Research Center
Hampton, VA

SUMMARY

The multigrid properties of two data reconstruction methods used for achieving second-order spatial accuracy when solving the two-dimensional Euler equations are examined. The data reconstruction methods are used with an implicit upwind algorithm which uses linearized backward-Euler time-differencing. The solution of the resulting linear system is performed by an iterative procedure. In the present study only regular quadrilateral grids are considered, so a red-black Gauss-Seidel iteration is used. Although the Jacobian is approximated by first-order upwind extrapolation, two alternative data reconstruction techniques for the flux integral that yield higher-order spatial accuracy at steady state are examined. The first method, probably most popular for structured quadrilateral grids, is based on estimating the cell gradients using one-dimensional reconstruction along curvilinear coordinates. The second method is based on Green's theorem. Analysis and numerical results for the two-dimensional Euler equations show that data reconstruction based on Green's theorem has superior multigrid properties as compared to the one-dimensional data reconstruction method.

INTRODUCTION

Multigrid methods have become a popular tool for obtaining steady solutions of the Euler or Navier-Stokes equations. Although true multigrid performance is difficult to obtain, there is no doubt that multigrid methods can significantly decrease the computer time necessary for convergence. However, the gain in performance from a single grid algorithm is directly related to the type of smoothing operator used on each level. Although explicit methods may be simple to program and have a relatively small number of operation counts, the unconditional stability that implicit methods offer tends to greatly overcome their disadvantages. In addition, explicit time advancement methods generally do not exhibit good smoothing properties when used with higher-order upwind data reconstruction techniques for a system of equations.

In addition to the time advancement technique, the method of flux evaluation plays an important role in algorithm efficiency. One commonly used way to achieve higher order accuracy is to reconstruct the data on cell faces appropriately using the cell centered data. For grids which consist of logically rectangular cells, the most popular approach is to use simple one-dimensional curve fitting methods such as used by Anderson *et al.* [1]. The one-dimensional data reconstruction methods have been used with great success in two and three-dimensional CFD codes which use grids consisting of logically rectangular cells.

General fluid dynamics problems may require generating grids around complex shapes for which it is difficult to generate a single grid consisting of logically rectangular cells. Using multiple-block

grids to model complex geometries has been implemented with success using multigrid algorithms [2][3]. Another approach for generating grids around complex geometries is to use triangular elements. On unstructured triangular grids, however, data reconstruction methods based on Green's theorem are more prevalent since this does not require interpolation along a coordinate direction.

In reference [4] the authors presented a single grid stability analysis and numerical experiments of several different data reconstruction methods. In this paper, we extend this work to show the effect of the data reconstruction on multigrid performance. The Full-Approximation Scheme (FAS) multigrid method has been incorporated into a quadrilateral-based unstructured grid Euler solver using the implicit time marching method of reference [5].

GOVERNING EQUATIONS

The governing equations are the time-dependent Euler equations, which express the conservation of mass, momentum, and energy for an inviscid gas. The equations are given by

$$\frac{\partial \mathbf{Q}}{\partial t} + \frac{1}{A}\oint_{\Omega} \vec{\mathbf{F}} \cdot \hat{\mathbf{n}} d\Omega = 0 \tag{1}$$

where A is the area of the cell that is bounded by the contour Ω with the outward-pointing unit normal $\hat{\mathbf{n}}$. The state vector $\mathbf{Q}$ and the flux vectors $\vec{\mathbf{F}}$ are given as

$$\mathbf{Q} = \begin{bmatrix} \rho \\ \rho u \\ \rho v \\ e \end{bmatrix}, \quad \vec{\mathbf{F}} \cdot \hat{\mathbf{n}} = \begin{bmatrix} \rho U \\ \rho U u + p\hat{\mathbf{n}}_x \\ \rho U v + p\hat{\mathbf{n}}_y \\ (e+p)U \end{bmatrix} \tag{2}$$

where ρ is the density, u and v are the x and y components of the velocity, e is the energy per unit volume, p is the pressure, and U is the velocity in the direction of the outward pointing normal to the cell

$$U = \hat{\mathbf{n}}_x u + \hat{\mathbf{n}}_y v \tag{3}$$

The equations are closed with the equation of state for a perfect gas

$$p = (\gamma - 1)\left[e - \rho\left(u^2 + v^2\right)/2\right] \tag{4}$$

where γ is the ratio of specific heats.

TIME ADVANCEMENT ALGORITHM

The method used for accelerating the solution to steady state is the Full Approximation Scheme (FAS) multigrid method. The technique used for smoothing the errors on each grid level is based on the scheme described in reference [5] applied to a grid of quadrilateral cells. The method is an

implicit upwind algorithm that uses linearized backward-Euler time differencing. The cell-averaged solution vector $\mathbf{Q}$ is updated at each time level n with the equations

$$\mathbf{L}^n \Delta \mathbf{Q}^n = -\mathbf{R}(\mathbf{Q}^n) \tag{5}$$

$$\mathbf{Q}^{n+1} = \mathbf{Q}^n + \Delta \mathbf{Q}^n \tag{6}$$

The operator $\mathbf{R}(\mathbf{Q}^n)$ is the discrete approximation to the flux integral in equation (1) at time level n. The fluxes are evaluated with Van Leer flux-vector splitting [6] and are second-order accurate if a linear data reconstruction method is used. The operator $\mathbf{L}^n$ is written as

$$\mathbf{L}^n = \frac{A}{\Delta t}\mathbf{I} + \frac{\partial \mathbf{R}^n}{\partial \mathbf{Q}^n} \tag{7}$$

To minimize the bandwidth and maintain block-diagonal dominance of the matrix $\mathbf{L}^n$, the Jacobian $\partial \mathbf{R}^n / \partial \mathbf{Q}^n$ is approximated by first-order upwind differencing rather than by exactly linearizing the second-order right-hand side of equation (5). The steady-state solution remains second-order accurate. The solution of the linear system (5) is performed by an iterative procedure. In the present study, subiterations are performed using red-black Gauss-Seidel where the flux-Jacobians in equation (7) are frozen at the current time level. It is recognized that the linear system must be solved adequately to gain the full benefits of an implicit formulation. However, the scope of this work is to analyze the effects of various data reconstructions to compute the right-hand side of equation (5). The stability and smoothing analysis presented later assumes the linear system is solved exactly at each time step.

UPWIND STENCILS

All of the reconstruction stencils used for the right-hand side of equation (5) in this study are based on MUSCL-type differencing [6]. In this approach, the flux vector $\vec{\mathbf{F}}$ is split into two components

$$\vec{\mathbf{F}} \cdot \hat{\mathbf{n}} = \hat{\mathbf{F}}\left(\mathbf{Q}^+, \mathbf{Q}^-\right) = \hat{\mathbf{F}}^-\left(\mathbf{Q}^+\right) + \hat{\mathbf{F}}^+\left(\mathbf{Q}^-\right) \tag{8}$$

where

$$\mathbf{Q}^{\pm}_{\text{face}} = \mathbf{Q}^{\pm}_{\text{cell}} + \Theta^{\pm}(\mathbf{Q}) \tag{9}$$

The values of $\mathbf{Q}$ are determined on each side of a cell face by using an interpolation operator Θ, and reconstructing the cell-centered data on each face as shown in figure 1. Upwind fluxes are computed from the two face values with Van Leer flux-vector splitting [6]. The stencils that are considered differ in the interpolation operator Θ.

One of the most common methods of data reconstruction for upwind structured flow solvers is to interpolate the data to the cell face using only the cells along the curvilinear coordinate direction which is perpendicular to the face [1]. Using the cell numbering shown in figure 2, a family of schemes is given by

$$\mathbf{Q}^{-}_{\text{face}} = \mathbf{Q}_2 + \frac{1}{4}[(1-\kappa)\Delta_- + (1+\kappa)\Delta_+]\mathbf{Q}_2 \tag{10}$$

$$\mathbf{Q}^{+}_{\text{face}} = \mathbf{Q}_3 - \frac{1}{4}[(1+\kappa)\Delta_- + (1-\kappa)\Delta_+]\mathbf{Q}_3 \tag{11}$$

where

$$\Delta_+\mathbf{Q}_i = \mathbf{Q}_{i+1} - \mathbf{Q}_i \tag{12}$$

$$\Delta_-\mathbf{Q}_i = \mathbf{Q}_i - \mathbf{Q}_{i-1} \tag{13}$$

These formulas assume the grid has been transformed from physical (x, y) space to computational (ξ, η) space where the grid spacing ($\delta\xi$, $\delta\eta$) is unity. Using this family of schemes as the interpolation operator results in the flux integration in a cell depending on a total of 9 cells for $-1 \le \kappa < 1$ as shown in figure 3.

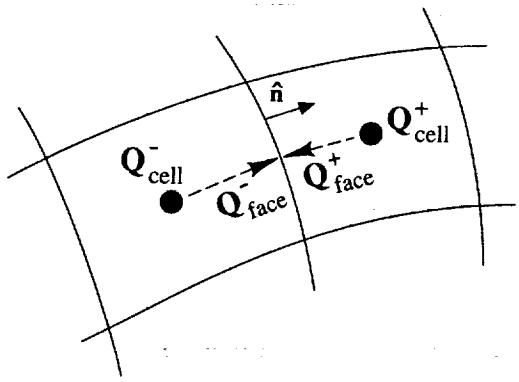

Figure 1. Data reconstruction for upwind fluxes

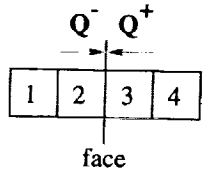

Figure 2. Cell Numbering for κ Methods

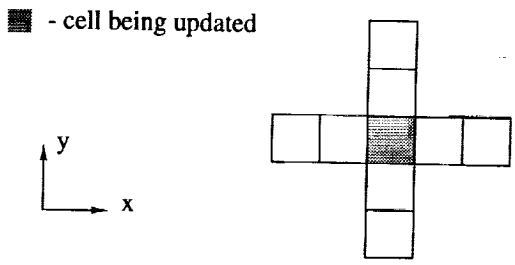

Figure 3. 9-point stencil

We can examine the relation between the discrete equations (10) - (13) and equation (8) by expanding the terms of the equations in a Taylor's series. Examining the interpolation of $\mathbf{Q}^-$ along a ξ coordinate line, a Taylor's series expansion about cell 2 is written as

$$\mathbf{Q}^-_{\text{face}} = \mathbf{Q}_2 + \Delta\xi \left.\frac{\partial \mathbf{Q}}{\partial \xi}\right|_{\xi=\xi_2} + \frac{(\Delta\xi)^2}{2} \left.\frac{\partial^2 \mathbf{Q}}{\partial \xi^2}\right|_{\xi=\xi_2} + \cdots \tag{14}$$

If $\kappa = 0$, a central difference across cell 2 is used to calculate the gradient so that

$$\Theta^-(\mathbf{Q}) = \Delta\xi \left.\frac{\partial \mathbf{Q}}{\partial \xi}\right|_{\xi=\xi_2} \approx \left(\frac{1}{2}\right)\left(\frac{\mathbf{Q}_3 - \mathbf{Q}_1}{2}\right) \tag{15}$$

For $\kappa = -1$, the gradient is approximated using only one-sided information

$$\Theta^-(\mathbf{Q}) = \Delta\xi \left.\frac{\partial \mathbf{Q}}{\partial \xi}\right|_{\xi=\xi_2} \approx \frac{1}{2}(\mathbf{Q}_2 - \mathbf{Q}_1) \tag{16}$$

Although not considered in this study, if $\kappa = 1/3$, the first and second derivatives of equation (14) are estimated with central differences which yield a spatially third-order accurate steady-state solution in one dimension.

The other stencil used in constructing the data on the face is based on Green's theorem. This was used for triangular grids by Barth and Jespersen [7] and Frink [8]. This method of data reconstruction was also used by Anderson [5] on triangular grids in conjuction with the implicit scheme shown here. The interpolation operator is evaluated in physical (x, y) space and is written as

$$\Theta^{\pm}(\mathbf{Q}) = (\nabla \mathbf{Q} \cdot \mathbf{r})^{\pm} \tag{17}$$

where $\nabla \mathbf{Q}$ is the average gradient in the cell and is evaluated using Green's theorem.

$$\begin{aligned} \frac{\partial \mathbf{Q}}{\partial x} &= \frac{1}{A} \oint_{\Omega} (\mathbf{Q}) \hat{\mathbf{n}}_x \, d\Omega \\ \frac{\partial \mathbf{Q}}{\partial y} &= \frac{1}{A} \oint_{\Omega} (\mathbf{Q}) \hat{\mathbf{n}}_y \, d\Omega \end{aligned} \tag{18}$$

To evaluate this numerically, inverse-distance weighting is used to transfer the cell-averaged data to the nodes [8].

$$\mathbf{Q}_{\text{node}} = \frac{\displaystyle\sum_{i=1}^{4} \frac{\mathbf{Q}_{\text{cell}_i}}{r_i}}{\displaystyle\sum_{i=1}^{4} \frac{1}{r_i}} \tag{19}$$

where r_i is the distance from the i-th cell center to the node. This reduces to simple averaging for uniform grids. Next, the trapezoidal rule is used to integrate around the cell. The x-component is given by

$$(\nabla \mathbf{Q})_x \approx \frac{1}{A_{\text{cell}}} \sum_{i=1}^{4} \left(\frac{\mathbf{Q}_{\text{node}_1} + \mathbf{Q}_{\text{node}_2}}{2} \right) \Delta s_{\text{face}_i} \hat{\mathbf{n}}_x \tag{20}$$

Here, A is the area of the cell, node_1 and node_2 define face_i, Δs is the length of face_i, and $\hat{\mathbf{n}}_x$ is the x-component of the outward pointing unit normal. The data on the cell faces is then determined using (17) where the position vector, $\mathbf{r}$, is computed from the cell center to the face center. Using Green's theorem and the trapezoidal rule results in a stencil of 21 cells for the flux integration. The complete procedure for determining $\mathbf{Q}$ values on the cell faces is shown in figure 4.

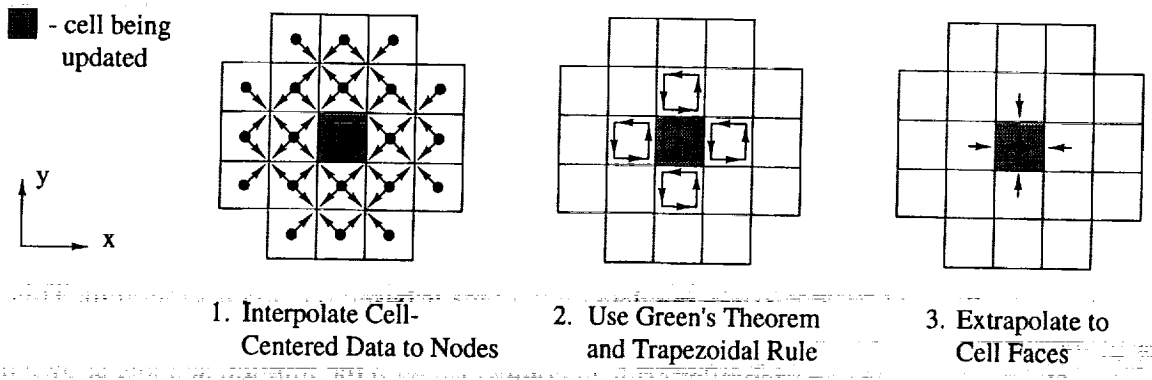

Figure 4. Data Reconstruction Using Green's Theorem

TRUNCATION ERROR

A truncation error analysis for the 9-point stencils using $\kappa = 0$ and $\kappa = -1$ as well as the 21-point stencil has been shown in reference [4] and is summarized here for completeness. The truncation error of each of the three stencils is examined by considering the semi-discrete approximation to a scalar advection equation with non-negative coefficients a and b.

$$\frac{\partial u}{\partial t} + a\frac{\partial u}{\partial x} + b\frac{\partial u}{\partial y} = 0 \tag{21}$$

This linear equation is a simplified model of the two-dimensional Euler equations.

Leaving the equation continuous in time, the spatial derivatives are approximated by each stencil and expanded in a Taylor series about the point being updated. The 9-point stencil with $\kappa = -1$ leads to the following equation:

$$\frac{\partial u}{\partial t} = -a\frac{\partial u}{\partial x} - b\frac{\partial u}{\partial y} + \frac{1}{3}\left(a\delta x^2 \frac{\partial^3 u}{\partial x^3} + b\delta y^2 \frac{\partial^3 u}{\partial y^3} \right)$$
$$-\frac{1}{4}\left(a\delta x^3 \frac{\partial^4 u}{\partial x^4} + b\delta y^3 \frac{\partial^4 u}{\partial y^4} \right) + h.o.t. \tag{22}$$

where δx and δy are the grid spacing in the x and y directions, respectively. The difference approximation is second order in the grid spacing with a dispersive leading truncation error term. The approximation is also dissipative, as can be seen from the fourth-derivative term of the truncation error. For an advection velocity that is aligned with the grid (a or $b = 0$), the dissipative term reduces to a fourth derivative in the flow direction.

For the 9-point stencil with $\kappa = 0$ we get the following equation:

$$\frac{\partial u}{\partial t} = -a\frac{\partial u}{\partial x} - b\frac{\partial u}{\partial y} + \frac{1}{12}\left(a\delta x^2 \frac{\partial^3 u}{\partial x^3} + b\delta y^2 \frac{\partial^3 u}{\partial y^3} \right)$$
$$-\frac{1}{8}\left(a\delta x^3 \frac{\partial^4 u}{\partial x^4} + b\delta y^3 \frac{\partial^4 u}{\partial y^4} \right) + h.o.t. \tag{23}$$

This equation differs from equation (22) in the magnitude of the coefficients of the dispersive and dissipative terms. We expect this difference formula to be less dissipative than the fully-upwind stencil.

A Taylor series expansion of the 21-point node-averaged stencil for the scalar advection equation gives the following:

$$\frac{\partial u}{\partial t} = -a\frac{\partial u}{\partial x} - b\frac{\partial u}{\partial y} + \frac{1}{12}\left(a\delta x^2 \frac{\partial^3 u}{\partial x^3} + b\delta y^2 \frac{\partial^3 u}{\partial y^3} \right)$$
$$-\frac{1}{8}\left(a\delta x \frac{\partial^2}{\partial x^2} + b\delta y \frac{\partial^2}{\partial y^2} \right)\left(\delta x^2 \frac{\partial^2 u}{\partial x^2} + \delta y^2 \frac{\partial^2 u}{\partial y^2} \right) + h.o.t. \tag{24}$$

This equations looks remarkably similar to equation (23), as the coefficients of the dispersive and dissipative terms are identical. However, the dissipative term of the 21-point stencil contains cross derivatives and looks similar to a biharmonic term. Note that even for a grid-aligned advection velocity the cross-derivative term does not vanish. We expect that this difference stencil, although of the same formal accuracy as the 9-point stencil, will be more dissipative.

STABILITY ANALYSIS

The basic stability properties of the upwind stencils considered here were examined in reference [4]. A Von Neumann analysis is used to examine the stability and convergence properties of the 9-point $\kappa = 0$ and $\kappa = -1$ stencils and the 21-point stencil. For each of the stencils, the equations are discretized according to equations (5) to (7). The operator $\mathbf{L}^n$ is obtained by first-order interpolation in all cases, and the right-hand side $\mathbf{R}(\mathbf{Q}^n)$ is obtained with the three second-order stencils.

Although the Von Neumann analysis is commonly applied to the scalar advection equation, we examine the stability of the system obtained by linearizing the Euler equations about a constant state, similar to the work in reference [5]. Applying a Fourier transform in space to the solution vector $\mathbf{Q}^n$ gives the equation

$$\mathbf{Q}^n = z^n \hat{\mathbf{Q}}_0 \exp(i\phi)\exp(i\psi) \tag{25}$$

where $\phi = \pi x/\delta x$, $\psi = \pi y/\delta y$ are the Fourier modes in the x and y directions, respectively, and z is the amplification factor. Substitution of this expression into (5) yields the following equation

$$\hat{\mathbf{L}}\left\{(z-1)\hat{\mathbf{Q}}_0\right\} = -\hat{\mathbf{R}}\left\{\hat{\mathbf{Q}}_0\right\} \tag{26}$$

where $\hat{\mathbf{L}}$ and $\hat{\mathbf{R}}$ are the Fourier symbols of the left- and right-hand-side operators for the constant-coefficient problem. Equations (25) and (26) lead to a generalized eigenvalue problem for z. By rearranging terms, we define the amplification matrix

$$\hat{\mathbf{G}} = \mathbf{I} - \hat{\mathbf{L}}^{-1}\hat{\mathbf{R}} \tag{27}$$

and z is an eigenvalue of $\hat{\mathbf{G}}$. The amplification matrix is 4 x 4 and complex; a necessary condition for stability is that the magnitude of the eigenvalues of $\hat{\mathbf{G}}$ are less than one for all ϕ and ψ. We will refer to the amplification factor for a given mode as the magnitude of the largest eigenvalue for that mode. The matrix $\hat{\mathbf{G}}$ depends upon four parameters: the Mach number; the flow direction; the CFL number, defined here as $c\delta t/\delta x$, where c is the speed of sound; and the cell aspect ratio, $\delta y/\delta x$.

The eigenvalue problem was solved numerically for a series of Fourier modes ϕ and ψ in the range $[-\pi, \pi]$. Below we show the amplification factors for a Mach number of 0.8, flow aligned with the grid in the x-direction, a CFL number of 100, and a cell aspect-ratio of 1. These results are typical of the stability properties of the implicit scheme at other Mach numbers.

Shown in figure 5 are the amplification factors for the 9-point stencil with $\kappa = -1$ and $\kappa = 0$ for a CFL of 100. This CFL number represents the asymptotic behavior for the three stencils considered here as shown in reference [4]. Note that the fully-upwind scheme ($\kappa = -1$) has very poor damping of the short-wavelength modes. As CFL $\rightarrow \infty$ the amplification factor of the $\phi = \pm\pi$ mode asymptotically approaches 1. Although unconditionally stable, the scheme is a very poor smoother for an FAS multigrid scheme using high CFL numbers. On the other hand, the upwind-biased stencil ($\kappa = 0$) leads to a scheme with excellent smoothing properties. All the Fourier modes are very well damped; in particular, the checkerboard and sawtooth modes have an amplification factor that tends to 0 with increasing CFL numbers. This scheme appears to be a very good multigrid smoother.

By using the 21-point stencil to discretize the steady-state operator we get even better stability properties, as is seen in figure 6. All the high-frequency modes are damped extremely well; the amplification factor for $\phi, \psi = \pm\pi$ has an asymptote of 0, making this operator an excellent choice as a multigrid smoother.

Considering the 9-point, $\kappa = 0$ stencil and the 21-point stencil in the case where the flow is skew to the grid, we get the results shown in figure 7. In both cases the damping of the short wavelengths is

essentially unchanged. The damping of the long wavelengths is worse, however, and the deterioration is somewhat more noticeable for the 9-point stencil, particularly for the intermediate wavelengths. The 21-point stencil retains its excellent stability properties over a larger range of wavelengths.

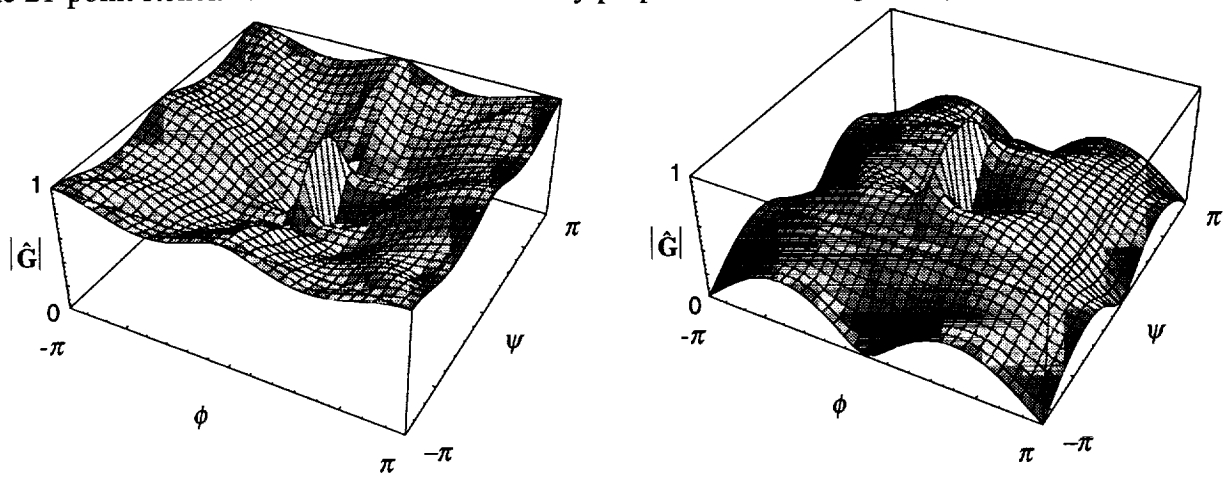

Figure 5. Amplification factors for 9-point stencil, Mach = 0.8, $\alpha = 0$, CFL = 100: $\kappa = -1$ (left) and $\kappa = 0$ (right)

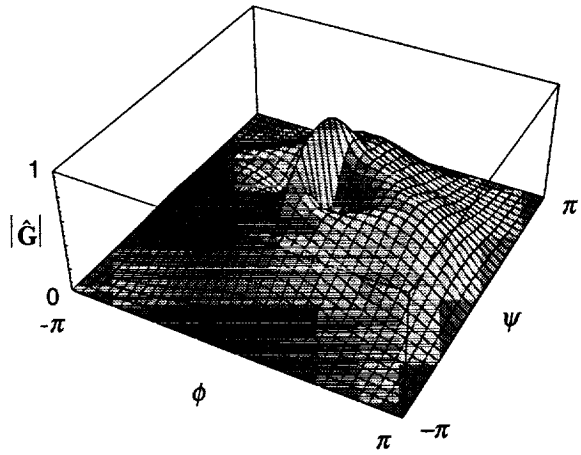

Figure 6. Amplification factor for 21-point stencil, Mach = 0.8, $\alpha = 0$, CFL = 100

Shown in figure 8 are the smoothing factors, defined as the maximum of the amplification factor over the range $\pi/2 < |\phi|, |\psi| < \pi$, and average amplification factors for the 9-point stencil over a range of CFL numbers from 1 to 1024 and κ from -1 to 1.The Mach number and flow angle are 0.8 and 45 degrees, respectively. These plots clearly show that the $\kappa = 0$ stencil has the best smoothing properties for the 9-point stencil.

A comparison of the smoothing and amplification factors for the 21-point and the 9-point, $\kappa = 0$ stencils is shown in figures 9 and 10. Shown in figure 9 are the smoothing and average amplification factors for flow aligned with the grid. Note that for CFL numbers up to about 16, the smoothing factors are identical. The asymptotic smoothing factors are slightly different: 0.524 and 0.563 for the 21-point and 9-point stencils, respectively. In contrast to the smoothing factors, the average amplification factor is about 50% lower for the 21-point stencil compared to the 9-point stencil. In figure 10 plots of

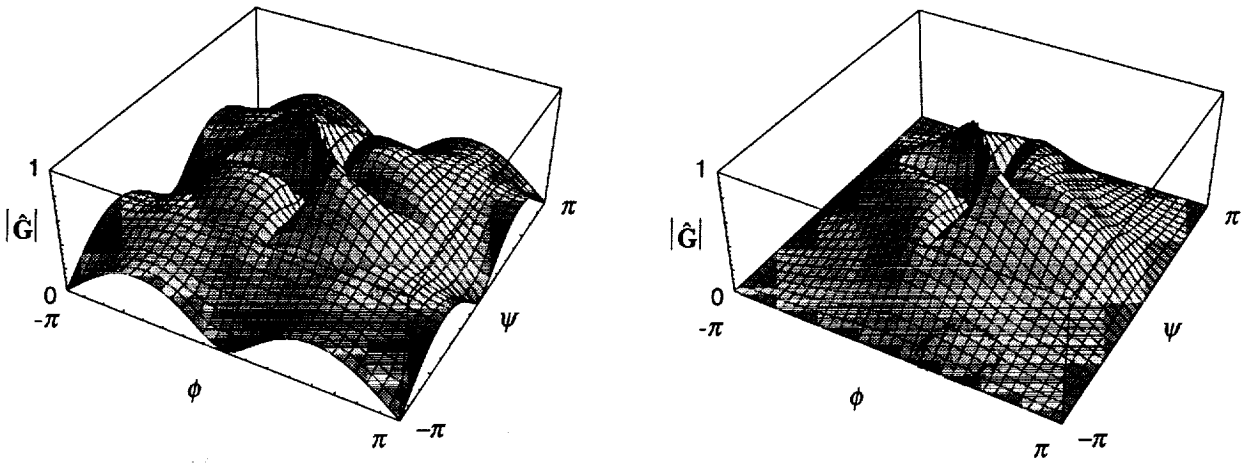

Figure 7. Flow at 45 degrees to the grid: 9-point stencil, Mach = 0.8, α = 45 degrees , CFL = 100: κ = 0 (left) and 21-point stencil (right)

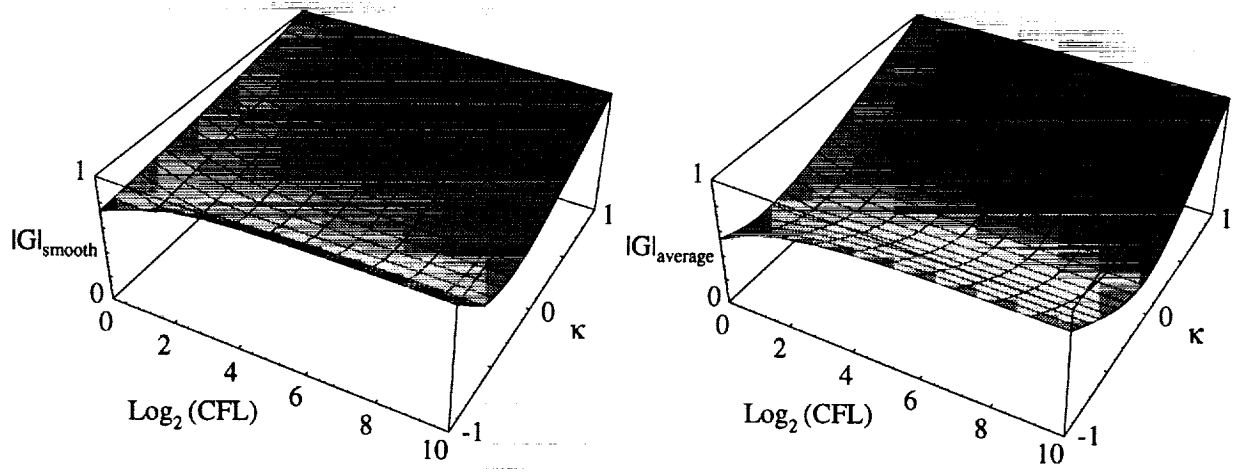

Figure 8. Smoothing factors and average amplification factors for κ methods

the smoothing factor and average eigenvalues are shown for both stencils for flow at 45 degrees to the grid. The average amplification factors are virtually unchanged, but there is some difference in the smoothing factors. The asymptotic values of the smoothing factors have deteriorated, increasing to 0.554 and 0.628 for the 21-point and 9-point stencils, respectively. The 21-point stencil's smoothing factor is less sensitive to the flow angle than that of the 9-point, κ = 0 stencil.

The effect of grid aspect ratio on the 21-point and 9-point κ = 0 stencil is shown in figure 11. Note that there is a large degradation in the smoothing properties for the 9-point κ = 0 stencil when using high aspect ratio cells such as those in a viscous calculation near a solid wall or wake region. The 21-point stencil, however, is generally not affected by the cell aspect ratio. This insensitivity of the smoothing factor as the flow angle and grid aspect ratio changes means that we expect that it will result in more uniform multigrid performance than the 9-point, κ = 0 stencil, over a variety of flow conditions and grid topologies.

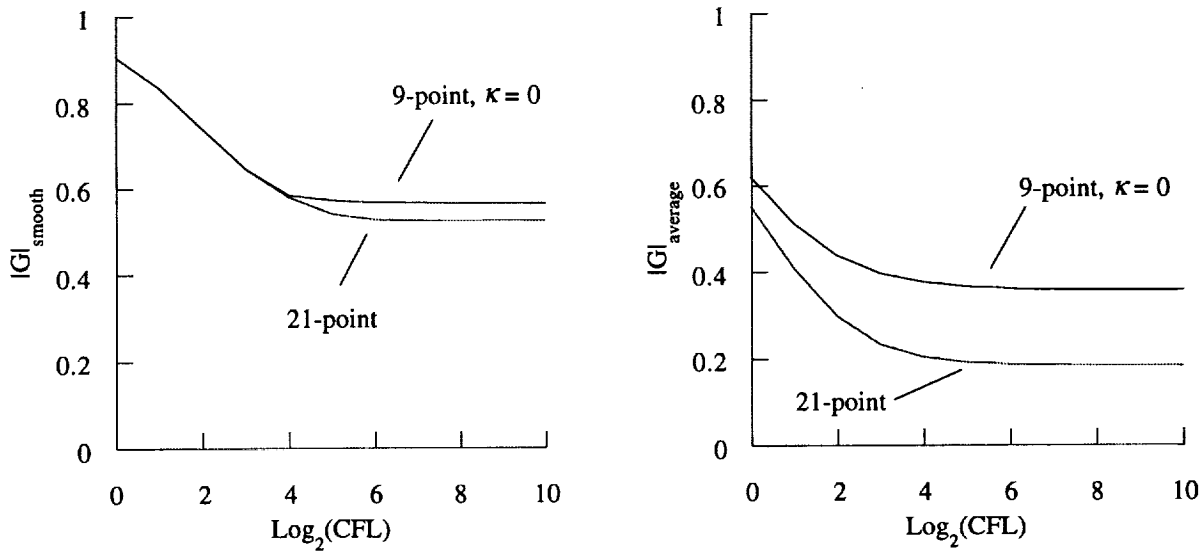

Figure 9. Smoothing factors and average amplification factors for the 21-point stencil and the 9-point stencil, $\kappa = 0$, for a flow angle of 0 degrees

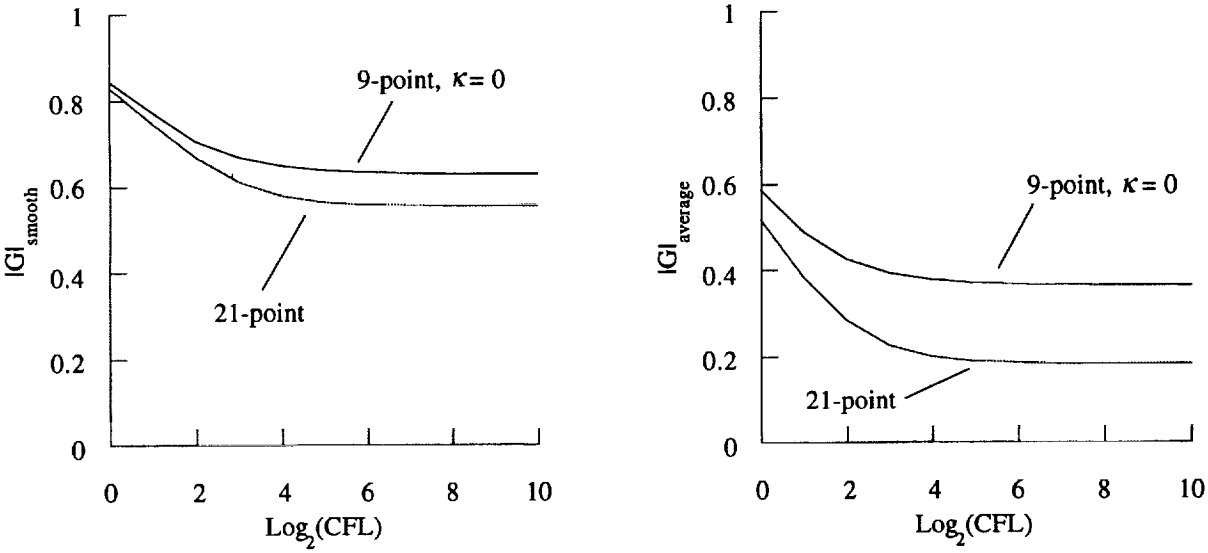

Figure 10. Smoothing factors and average amplification factors for the 21-point stencil and the 9-point stencil, $\kappa = 0$, for a flow angle of 45 degrees

EULER RESULTS

Results for the two-dimensional Euler equations are now presented. Two test cases are used in this study. The first case is the subsonic flow in a channel with a 3% $\sin^2 x$ bump. This case was chosen because the flow is nearly grid aligned in every cell. The channel length is three times the channel height and the length of the bump is equal to the channel height. A freestream Mach number of 0.3 is used. The grid used in this study consists of 157 points along the wall and 49 points normal to the

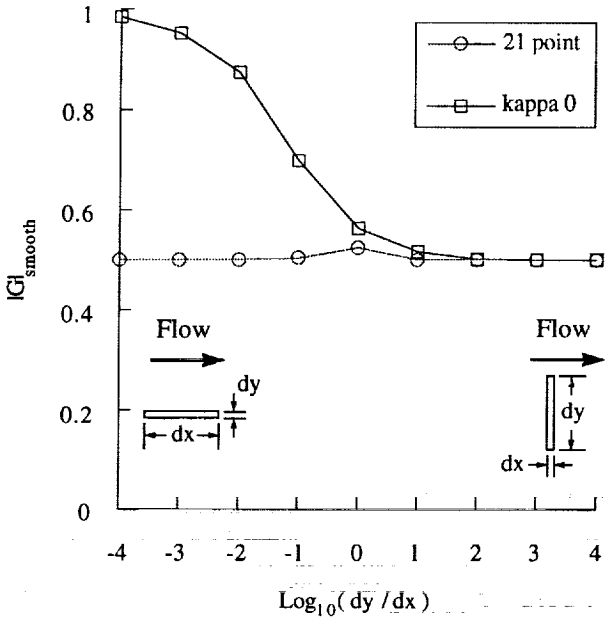

Figure 11. Effect of Grid Aspect Ratio on Smoothing Factor for Flow Aligned with Grid

wall and is shown in figure 12. The density contours for the converged solution using the 21-point stencil are also shown in figure 12. All of the cases utilize a 3-level V-cycle using 15 subiterations to solve the linear system at each level. One smoothing iteration is performed on each level except the coarsest grid where 3 smoothing steps are performed.

Convergence histories for this case using the 9-point stencil with $\kappa = -1$ are shown in figure 14a. As the CFL increases, the convergence rate improves up to a CFL of about 10 after which the convergence degrades, eventually becoming unstable. As discussed above, when the CFL is increased, high frequency error modes approach neutral stability. The analysis, however, assumes the linear system is solved exactly at each time step which is generally not the case with only 15 subiterations. Therefore, the scheme may require a prohibitive number of subiterations to remain stable at high CFL numbers.

The convergence histories for the 9-point stencil with $\kappa = 0$ are shown in figure 14b. Unlike the 9-point stencil with $\kappa = -1$, this stencil produces very good convergence rates as the CFL is increased. Note that there is little decrease in the spectral radius after a CFL of 100. This is consistent with the analysis shown in figure 10. The convergence histories for the 21-point stencil are shown in figure

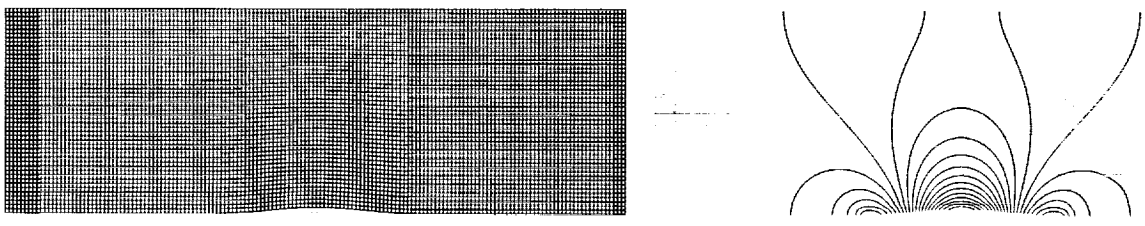

Figure 12. 3% $Sin^2(x)$ bump grid and contours

14c and are very similar to the 9-point, $\kappa = 0$ stencil. For this test case, in which the flow is aligned with the grid, both stencils have very good convergence properties.

To examine the behavior of the schemes with higher aspect ratio cells and when the flow is not aligned with the grid, a second test case is considered which is a NACA 0012 airfoil in a Mach = 0.8 freestream at 0 degrees angle-of-attack. The calculations were performed on a 65x25 c-grid which is shown in figure 13 along with the converged density contours obtained with the 21-point stencil. All cases were run using a 3-level V-cycle and 20 subiterations to solve the linear system.

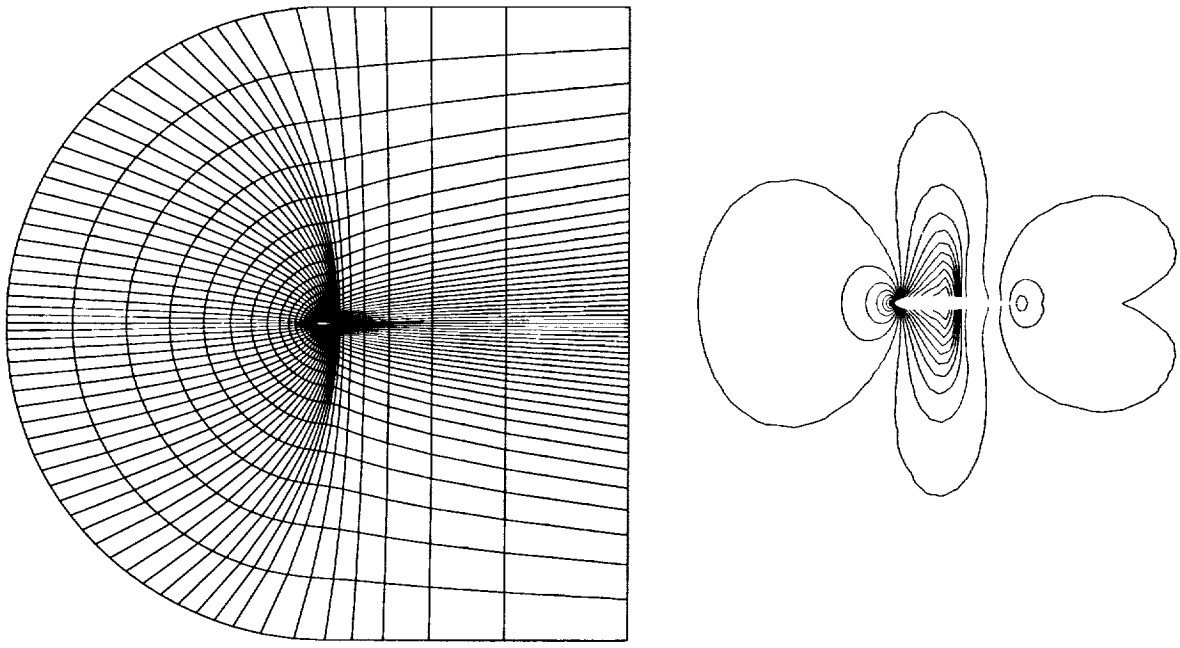

Far Field Grid Near Field Density Contours

Figure 13. NACA 0012, Mach = 0.8, $\alpha = 0^{o}$ grid and contours

The convergence histories for both the 21-point stencil and 9-point stencil with $\kappa = 0$ are shown in figure 14d. Only the $\kappa = 0$ value is used because of the poor convergence properties of the $\kappa = -1$ stencil. As shown, the 21-point stencil converges significantly faster than the 9-point $\kappa = 0$ stencil. In particular, note that the number of multigrid cycles to reach a residual of 10^{-16} using the 21-point stencil is about the same as for the channel flow. By contrast, the 9-point, $\kappa = 0$ stencil shows a marked deterioration in performance compared to the channel flow case. These results are consistent with the analysis for flow angularity and cell aspect ratio effect presented above.

DISCUSSION

The analysis and computations presented indicate that the choice of data reconstruction for upwind methods can have a substantial effect on the multigrid performance for a given time advancement scheme. In particular, the popular 9-point, $\kappa = -1$ stencil exhibits very poor multigrid conver-

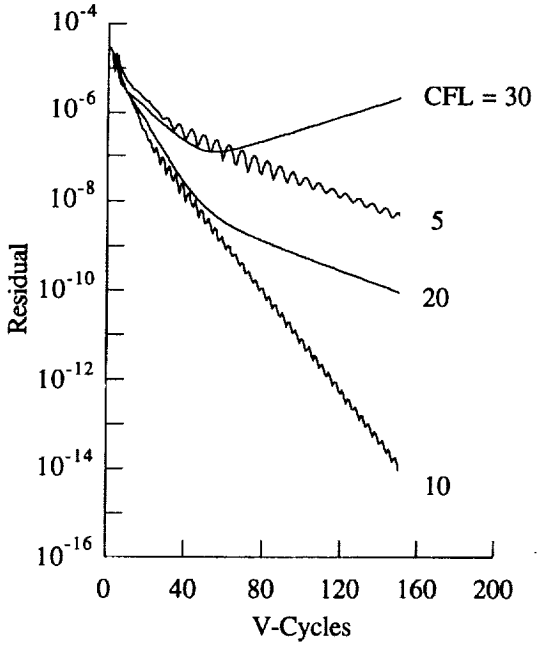

a) Sin²x bump, 9-point, κ = -1 stencil

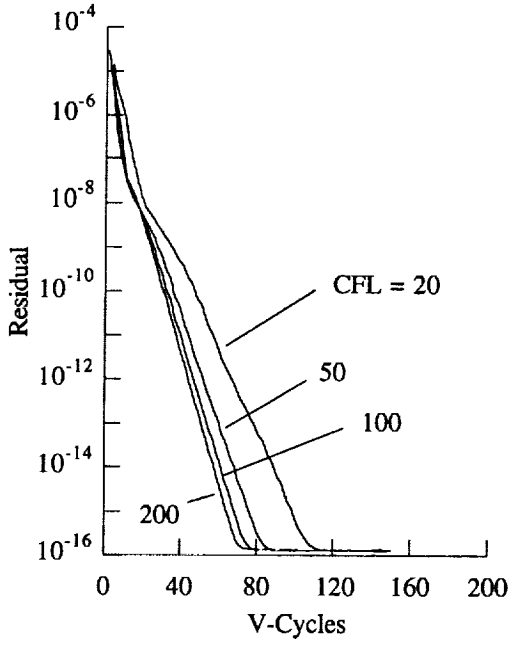

b) Sin²x bump, 9-point, κ = 0 stencil

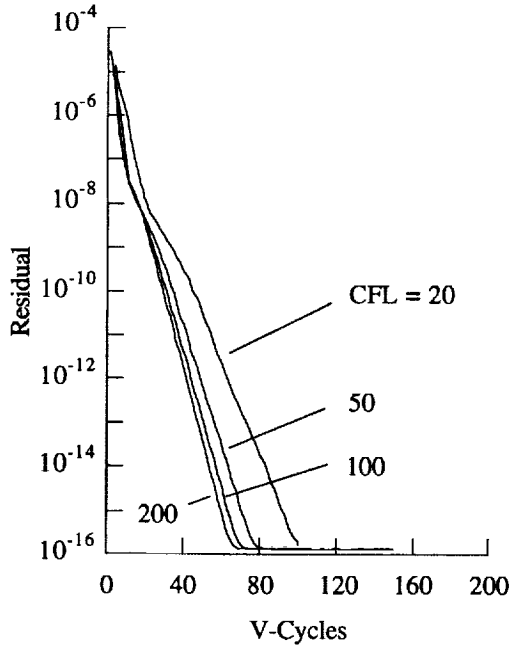

c) Sin²x bump, 21-point stencil

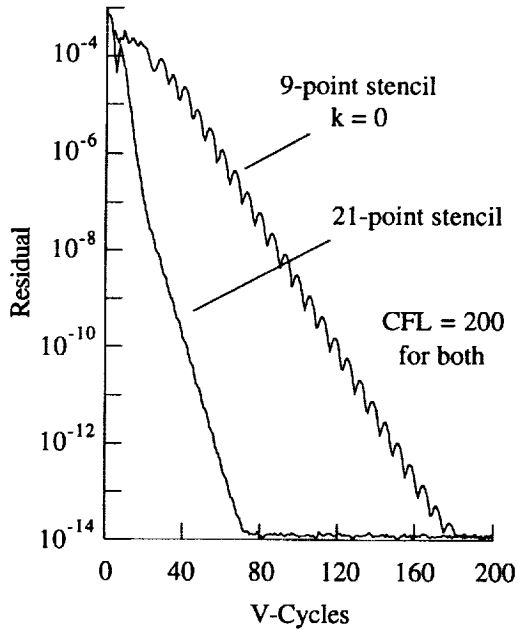

d) Transonic airfoil, 21-point and 9-point, κ = 0 stencil

Figure 14. Residual Histories

gence for high CFL numbers. The 9-point, $\kappa = 0$ stencil has much better smoothing properties but still has difficulty damping the high frequency waves if the flow is not aligned with the grid. By using an interpolation operator based on Green's theorem, excellent smoothing properties are obtained for high CFL numbers regardless of the flow angularity as shown in figures 9 and 10. This has been shown through analysis and confirmed through numerical experiments.

REFERENCES

1. Anderson, W. K., Thomas, J. L., and Van Leer, B., "A Comparison of Finite Volume Flux Vector Splitting for the Euler Equations," *AIAA J.*, Vol. 24, No. 9, Sept. 1986, pp. 1453–1460.
2. Vatsa, V. N., Sanetrik, M. D., and Parlette, E. B., "Development of a Flexible and Efficient Multigrid-Based Multiblock Flow Solver," AIAA Paper 93-0677, January 1993.
3. Ghaffari, F., Luckring, J. M., Thomas, J. L., and Bates, B. L., "Navier-Stokes Solutions About the F/A-18 Forebody-Leading-Edge Extension Configuration," *Journal of Aircraft*, Vol. 27, pp. 737-748, 1990.
4. Roberts, T. W. and Warren, G. P., "Analysis of Implicit Second-Order Upwind-Biased Stencils," AIAA Paper 93-3379, June 1993.
5. Anderson, W. K., "Grid Generation and Flow Solution Method for Euler Equations on Unstructured Grids," NASA Technical Memorandum 4295, April 1992.
6. Van Leer, B., "Flux Vector Splitting for the Euler Equations," *Lecture Notes in Physics*, Vol. 170, pp. 501–512, 1982.
7. Barth, T. J., and Jespersen, D. C., "The Design and Application of Upwind Schemes on Unstructured Meshes," AIAA Paper 89-0366, January 1989.
8. Frink, N. T., "Upwind Scheme for Solving the Euler Equations on Unstructured Tetrahedral Meshes," *AIAA J.*, Vol. 30, No. 1, Jan. 1992, pp. 70-77.
9. Mulder, W. A., and Van Leer, B., "Experiments with Implicit Upwind Methods for the Euler Equations," *J. Comput. Phys.*, Vol. 59, No. 2, June 1985, pp. 232–246.